Research Article | Vol. 3, No. 9 / 15 September 2020 / OSA Continuum 2332

Structural and optical characteristics of dysprosium-doped zinc zirconate nanocomposites

MICHAEL K. MUSEMBI,[1,2,*] FRANCIS B. DEJENE,[1] AND IORKYAA AHEMEN[1,3]

[1]Department of Physics, University of the Free State (QwaQwa campus) Private Bag, X13 Phuthaditjhaba, 9866, South Africa
[2]Department of Physical Sciences, Machakos University, P.O. BOX 136–90100, Machakos, Kenya
[3]University of Agriculture, Private Mail Bag 2373, Makurdi. City, Benue State, Nigeria
[*]mchmusembi@yahoo.com, +27642911410

Abstract: Zinc zirconate nanocomposites with varying compositions of Dy^{3+} ions were synthesized through a solution combustion method using citric acid as a fuel. There were mixed hexagonal ZnO and cubic ZrO_2 phases in the X-ray diffraction patterns of the composites whose average crystallite sizes range between 27 and 38 nm. Scanning electron microscopy images show a mixture of polygonal and hexagonal rod-like structures of varying aggregation levels at the different Dy^{3+} -doping concentrations. The reflectance spectra showed absorption edges around 400 nm and an energy bandgap between 2.99 and 3.07 eV. There was a violet emission from the host matrix that gradually shifted towards white light with enhanced doping. At a higher Dy^{3+} concentration, there was luminescence quenching attributed to dipole-dipole interaction among the dopant ions. The synthesized nanocomposite phosphors may be used in sensors and colored display technology.

1. Introduction

Zinc zirconate nanocomposites have been applied in dye-sensitized solar cells (DSSCs) as well as in the photocatalytic removal of textile dyes [1–4]. Nanocomposites exhibit more enhanced properties than those inherent in the individual constituent compounds. These properties are usually dominated by the interface or interphase characteristics [5,6]. In the zinc zirconate nanocomposites, the different percentages of ZnO and ZrO_2 compounds significantly affect the applications of the material [7]. In the nanocomposite, zinc oxide (ZnO) has been observed to enhance the conductivity and stability of the material [8]. Zinc oxide has drawn a lot of research attention due to its possible application in solar cells and water purification among other interests [2,3,9–11]. Further, the oxide has been used in chemical gas sensors, the removal of environmental contaminants and in photocatalysis. Due to its anti-bacterial activity, zinc oxide is used in the production of cosmetics and sunscreens [12].

The ninth most abundant substance in the earth's crust, zirconium, forms three major oxide phases; namely monoclinic, tetragonal and the cubic phase [13]. The properties of zirconium oxide (zirconia) depend on the phase that is present in a particular material. The thermal and chemical stability of zirconia coupled with excellent photophysical characteristics make it useful in the ceramics industry, dentistry, piezo-electric devices and as an electrolyte for electrochromic devices. With a high refractive index of about 2.18, zirconia is also used as a gemstone [13–16]. Due to a tunable wide bandgap of up to 6.4 eV, zirconia phosphors are a good host matrix for rare-earth ions and hence useful in light emitting applications as well as in high-temperature thermometry [17,18].

#393520 https://doi.org/10.1364/OSAC.393520
Journal © 2020 Received 26 Mar 2020; revised 11 Aug 2020; accepted 13 Aug 2020; published 18 Aug 2020

OSA CONTINUUM

Rare earth metal dopants are used in semiconductor nanocomposites in order to influence their structural and optical properties [15,19,20]. Dysprosium is a rare earth metal used in making contrast agents for magnetic resonance imagery and the production of permanent magnets for electric cars as well as direct-drive wind mills. It is also used in the manufacture of multi-layer ceramic capacitors and data storage materials such as computer hard disc drives [21–23].

The most traditional route for preparing perovskite nanomaterials is the solid-state reaction method. Nevertheless, ceramic material oxides prepared using this conventional method have shown inhomogeneity through uncontrolled and irregular particle morphologies [24,25]. In the recent past, there has been increased uptake of wet chemical synthesis methods. By reducing the diffusion path, wet chemical methods ensure molecular level mixing of each of the constituent compounds to the nanoscale. These methods have been used in the synthesis of semiconductor oxides of high crystallinity at lower temperatures in comparison to the conventional solid-state reactions [26].

Among the wet chemical methods, solution combustion synthesis (SCS) is an effective route for the synthesis of nanoparticles. Once heated, the precursor mixture results in a self-sustaining exothermic reaction, in which the reactants self-ignite. This method has gained prominence due to the simplicity of equipment and the refinement of the resultant nanocrystals [17,27–32]. Studies have reported the synthesis of zinc zirconate nanocomposites by sol-gel [4,7,33] and hydrothermal [34] techniques. This study sought to investigate the optical and structural characteristics of dysprosium-doped zinc zirconate nanocomposites, synthesized by citric acid - assisted solution combustion process which to the best of our knowledge, has not yet been investigated nor reported.

2. Experiment

2.1. Synthesis

The composite was synthesized using 80 wt. % zirconium butoxide in 1-butanol from Aldrich alongside 98% zinc nitrate, analytical grade nitric acid and ammonia solution from Merck. Details of the synthesis route used in the preparation of the composites are outlined in our earlier work [35,36]. The zirconium (IV) butoxide was reacted with concentrated nitric acid to produce a solution of zirconium nitrate. The solution was diluted with 50 ml of de-ionized water and then mixed with 0.03 M zinc nitrate. Six samples were made by mixing the solutions with varying percentages of dysprosium nitrate, constituting 0, 1, 2, 3, 4 and 5% Dy^{3+} ions per mole. Citric acid fuel which acted as a complexant, was added to each of the mixtures and then the pH adjusted, while stirring using ammonia solution to 7. In each case, the precursor mixture was heated until spontaneous flaming occurred as a result of self-combustion. Using a mortar and pestle, the resultant fluffy composite powders were ground, then calcined at 600 °C for 2 hours.

2.2. Characterization methods

X-ray diffraction (XRD) measurements on the composite were done using a Bruker D8 X-ray diffractometer whose wavelength, $K\alpha = 0.15406$ nm. The angle of diffraction, 2θ was varied between 10° and 70° in steps of 0.03° per minute. Ultraviolet/visible (UV-vis) measurements were performed using a Lambda 950 PerkinElmer UV WinLab Spectrophotometer while photoluminescence measurements were done with a Hitachi Spectrophotometer, Model number F-7000 FL. The morphology studies were carried out using a Jeol JSM-7800F Field Emission Scanning Electron Microscope (FESEM) equipped with Oxford Aztec EDS and Gatan Mono CL4.

OSA CONTINUUM

3. Results and discussion

3.1. X-ray diffraction analysis

Figure 1 shows XRD patterns of the synthesized nanocomposite mixtures of the cubic zirconia and the hexagonal zinc oxide phases that correspond to ICDD cards 81-1551 and 75-1526, respectively. From the figure, it was observed that the zirconia peaks were comparatively broader and more intense than the zinc oxide peaks. The enhanced peak intensity on increased doping was probably due to the more preferentially oriented reflecting surface planes that resulted from an increased density of the zirconia crystallites [37,38].

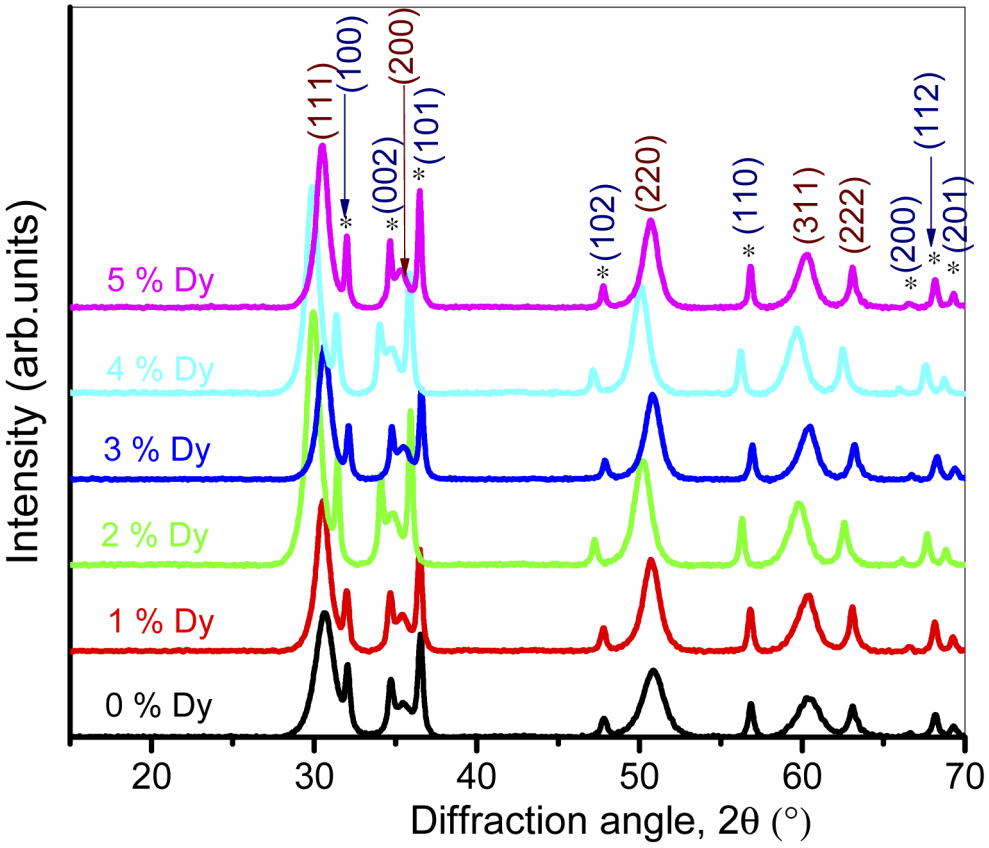

Fig. 1. XRD patterns of the Dy^{3+}-doped nanocomposites.

Figure 2 shows the peak shifts against the dopant concentrations. For each of the phases in the composite, there was an initial shift towards lower angles as a result of the incorporation Dy^{3+} at the cations sites. It was expected that the substitution of either Zn^{2+} or Zr^{4+} ions by the Dy^{3+} dopant would cause a distortion in the crystal and hence strain the lattice. Further, there would be a need for charge compensation due to the valence difference between the dopant and the substituted cations, leading to oxygen vacancy defects.

In the hexagonal ZnO, the Zn^{2+} ions are tetrahedrally coordinated by four O^{2-} ions while the Zn^{2+} ions coordinating each O^{2-} ion is four. Therefore, its coordination number (CN) in the structure is 4, and the ionic radii for the Zn^{2+} and Dy^{3+} ions at CN = 4 are equal to 0.60 Å and 0.78 Å, respectively [39,40]. Similarly, the cubic ZrO_2 structure has Zr^{4+} coordinated by 6-oxygen atoms and the Zr^{4+} ionic radii is 0.72 Å while that of Dy^{3+} is 0.91 Å [40]. The

OSA CONTINUUM

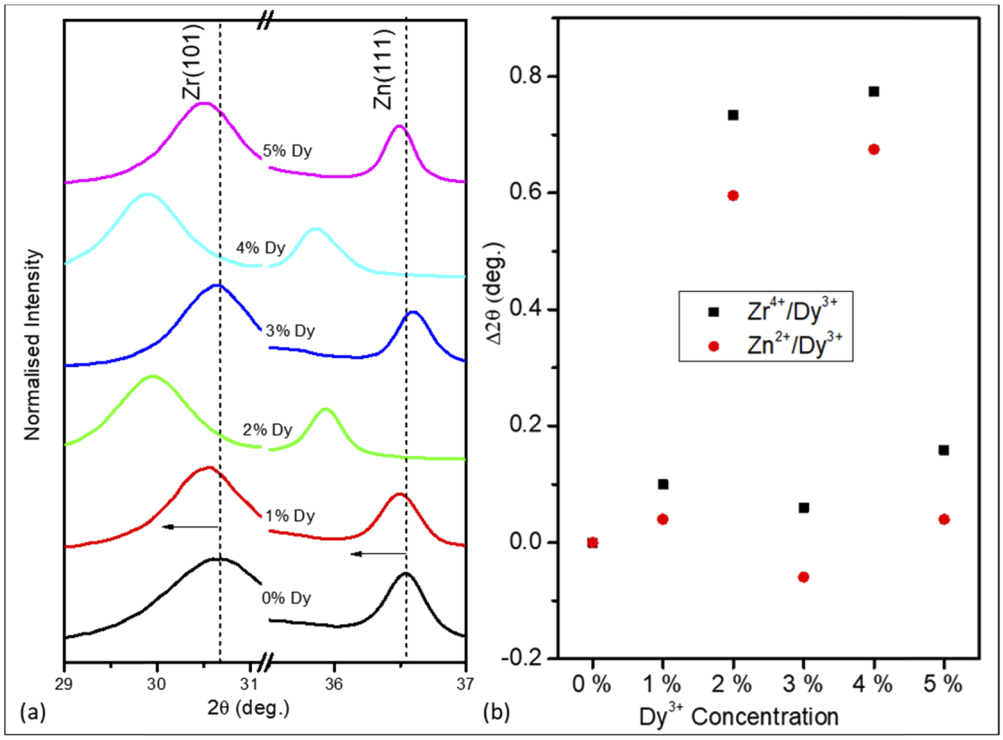

Fig. 2. (a) Illustration of (111) ZnO/Dy^{3+} & (101) ZrO_2/ Dy^{3+} peak shifts and (b) difference in peak shifts for ZrO_2 and ZnO, respectively for various Dy^{3+} ion concentrations.

differences in ionic radii between Zn^{2+}/Dy^{3+}, and Zr^{4+}/Dy^{3+} are 0.18 Å and 0.19 Å, respectively. These values are, however, are too close to pinpoint the substitution site for the Dy^{3+} dopant ions.

Earlier studies have shown that the radius percentage difference between dopant and the host ions should not be greater than 30%. For the nanocomposite, the difference in the percentage radius, r_i between the dopant ion (Dy^{3+}) and the host ions (Zn^{2+}) in ZnO and (Zr^{4+}) in ZrO_2, were evaluated using the relation [41,42];

$$r_i = \frac{r_h - r_d}{r_i} \times 100\ \% \tag{1}$$

where r_h is the host radius (Zn^{2+}or Zr^{4+}) and r_d is the radius of the Dy^{3+} dopant ion, at the coordination number, *CN*. When a Dy^{3+} ion substitutes a Zn^{2+} ion, the value of r_h is 30% and 26% when on a Zr^{4+} site. Therefore, the Dy^{3+} dopant will preferentially substitute the Zr^{4+} ions in the nanocomposite lattice because of the smaller radius percentage difference, despite the ionic radius difference. This is correlated by Fig. 2(b), which shows that with the incorporation of the Dy^{3+} in the nanocomposite structure, the ZrO_2 lattice is more distorted than that of ZnO.

The composite crystallite sizes and their corresponding lattice strains were determined using the relationships [43–46];

$$\beta_\varepsilon = 4\varepsilon\ tan\theta \tag{2}$$

$$\beta_D = \frac{k\lambda}{D\ cos\theta} \tag{3}$$

where D is the average size of the crystallites, ε is the micro-strain in the lattice, k is a shape dependent dimensionless factor, λ is the wavelength of the X-rays used, θ is the Bragg's angle of diffraction while β_ε and β_D are the micro-strain and crystal size profile broadening, respectively.

OSA CONTINUUM

These crystallite parameters were obtained using the following four most intense peaks in each phase; ZnO (100), (002), (101), (110) and ZrO_2 (111), (220), (311), (200). Table 1 shows the average crystallite size, micro-strain, lattice constants and the volume of the unit cell of the nanocomposites as calculated from those peaks [25,47]. Generally, the substitution of the larger ion (Dy^{3+}) at the sites of smaller ions (Zr^{4+} & Zn^{2+}) in the lattice caused an enlargement of the lattice and hence an increase in average crystallite size. The table shows that there were small deviations in the calculated values of the lattice constants and the volume of the unit cell for the Dy^{3+}- doped nanocomposites against those of the undoped sample, which were attributed to the local distortions on the crystal structures. The enlargement of the unit cell volume for the doped samples in comparison with the undoped sample is a confirmation of the presence of the Dy^{3+} on both cation sites in the nanocomposite lattice. Table 1 further reveals that the lattice strain of the nanocomposite samples decreases with increasing Dy^{3+} concentration (although non-monotonically). The occupation of Dy^{3+} ions on the tetrahedral sites of the host cations is therefore, expected to increase the lattice strain of the nanocomposite as a result of the difference in radii. The uneven redistribution of strain in the component lattices of the nanocomposite is attributed to lattice distortions arising from the change of the morphology of the particles [48].

Table 1. Values of the average crystallite size, lattice parameters and induced lattice strain of the nanocomposites

Sample	Nanocomposite Crystal size	Lattice Parameters ZnO			Lattice Parameters ZrO_2		Crystal Strain, ε (10^{-3})	
	(nm)	a(Å)	c(Å)	V(^{3})	a(Å)	V(^{3})	ZnO	ZrO_2
0% Dy	27.1	3.210	5.560	49.613	5.069	130.247	2.76	7.40
1% Dy	28.9	3.156	5.466	47.149	5.075	130.710	2.47	5.96
2% Dy	33.8	3.257	5.641	51.814	5.144	136.114	2.07	6.18
3% Dy	29.6	3.263	5.652	52.121	5.150	136.591	2.14	6.26
4% Dy	38.3	3.213	5.565	49.755	5.081	131.174	1.75	5.71
5% Dy	32.4	3.205	5.551	49.367	5.069	130.247	1.84	6.22

3.2. Composition and morphology studies

Figure 3 presents some Energy Dispersive X-ray Spectroscopy (EDS) spectra, that were selected to represent the host and doped samples of the nanocomposites. For the undoped sample in Fig. 3(a), the spectrum displays the presence of Zn, Zr, O peaks while the spectrum for the Dy^{3+}-doped sample (Fig. 3(b)) shows Dy peaks in addition to the other elements. The preferential substitution of Zr by Dy is confirmed by the reduced atomic percentage of Zr in the doped sample. It was also observed that there were no other impurity peaks present in the samples, apart from a carbon peak due to the tape used for holding the samples during the measurements.

Figure 4(a-f) present SEM images of Dy^{3+}-doped nanocomposite samples at the various dopant concentrations. Figure 4(a) shows well dispersed polygonal-shaped particles in the undoped nanocomposite. The images for the samples doped with Dy^{3+} at 1% and 3% in Fig. 4(b), (d) show similar characteristics with those of the undoped sample except that the particulates were more populated and compact than in Fig. 4(a). At 2% Dy^{3+} doping, Fig. 4(c) shows an agglomeration of vertically erect hexagonal rods. At 4% Dy^{3+}-doping (Fig. 4(e)), the particles transform into well packed aggregates of eroded polygons similar to those at 5% Dy^{3+} doping in Fig. 4(f), although the latter has smaller crystals that are less agglomerated. It was observed from the SEM images that inadequate or excess dopant concentration inhibits the growth of compact crystal structures. The variation of the morphology with doping was attributed to the lowering of the surface energy of the particles as well as the distortion of grain shapes [49,50].

OSA CONTINUUM

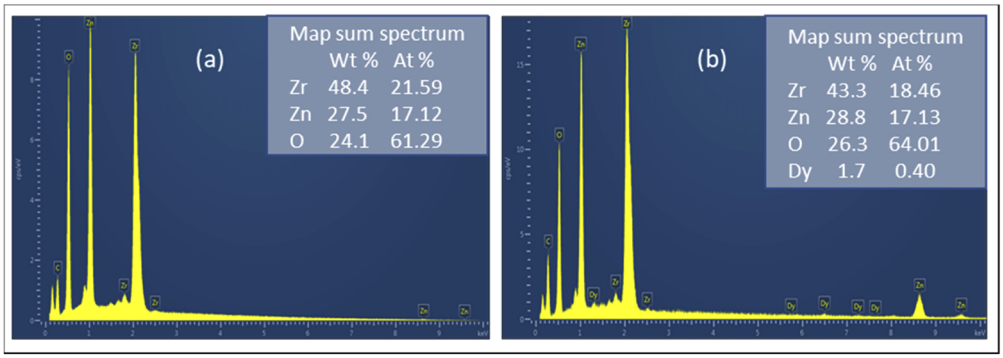

Fig. 3. Elemental composition spectra at (a) 0% Dy-doping, the host material (b) 4% Dy-doping ratio.

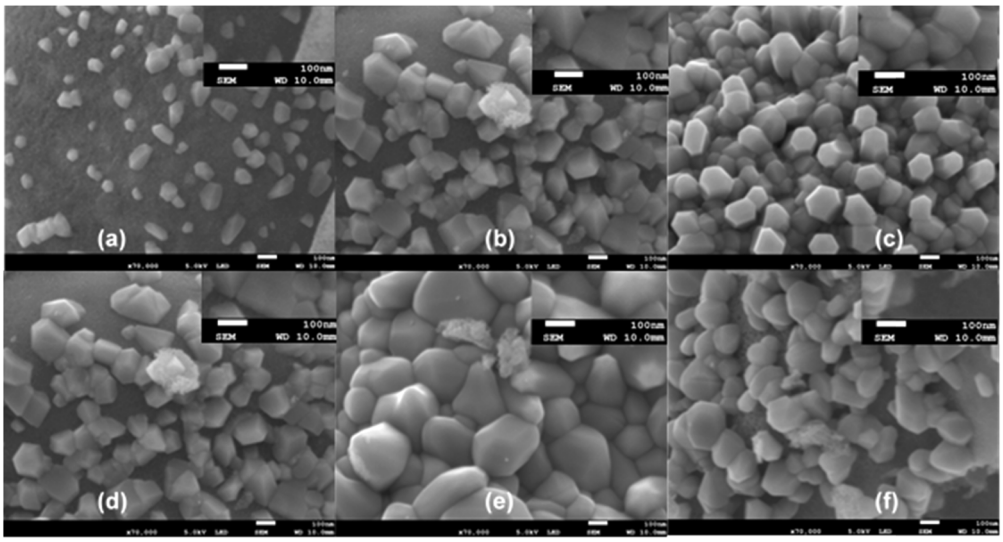

Fig. 4. SEM images of the nanocomposites with (a) 0%, (b) 1%, (c) 2% (d) 3% (e) 4% and (f) 5% of Dy^{3+} in the nanocomposite.

3.3. *Diffuse reflectance spectroscopy*

Figure 5(a) shows diffuse reflectance spectra of the nanocomposites. The non-monotonic variation in the reflectance as the dopant concentration changes showed absorption edges around 400 nm. By evaluating the Kubelka-Munk function, $F(R) = \frac{(1-R)^2}{2R}$ together with Tauc's relation on the spectra, the energy bandgap of the nanocomposites was determined [45,46]; For direct transition bandgap materials,

$$F(R)h\upsilon = \alpha_0(h\upsilon - E_g)^{1/2} \tag{4}$$

where R, $h\nu$, α_0, and E_g represent the absolute reflectivity, photon energy, absorption coefficient, and optical energy bandgap, respectively. As illustrated in Fig. 5(b), E_g was obtained by plotting $[F(R)h\nu]^2$ against $h\nu$ and then extrapolating the linear section of the curve to the $h\nu$-axis, the point where $[F(R)h\nu]^2 = 0$. The energy bandgaps were obtained as 3.07, 3.01, 3.04, 2.99, 3.03 and 3.04 eV for 0%, 1%, 2%, 3%, 4% and 5% Dy^{3+} concentrations, respectively. These bandgaps represented a trend which is in agreement with that of the crystallite sizes in Table 1.

OSA CONTINUUM

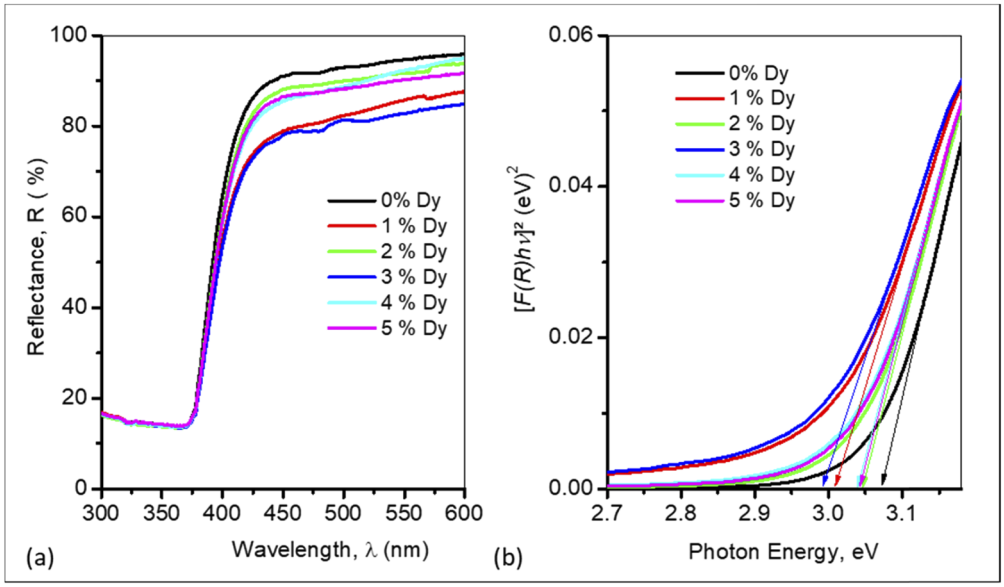

Fig. 5. (a) UV-vis reflectance spectra (b) a plot of the Kubelka-Munk function of the composite.

The declined energy bandgap of all doped samples relative to the undoped nanocomposite is an indication that Dy^{3+} formed energy states within the host bandgap. Generally, energy levels within the bandgap create shallow donor level of impurities near the edge of the conduction band while the levels near the valence band edge are created by shallow acceptor impurities. This means that there is an increase of the density of states of these dopant ions as the amount of doping increases, which effectively reduces the bandgap by the formation of a continuum of states, just as in the bands [51].

3.4. *Photoluminescence spectroscopy*

Figure 6(a) shows the photoluminescence excitation and emission spectra determined at various wavelengths for undoped zinc zirconate nanocomposite. The excitation spectra obtained by examining the sample at 406, 481 and 580 nm wavelengths shows three peaks. The dominant excitation peak observed at 211 nm was attributed to Zr^{4+} - O^{2-} charge transfer band, while those at 275 and 400 nm are due to defect levels in the host [52]. The presence of the host excitation peaks when monitoring the emission from Dy^{3+} at 481 and 580 nm is an indication that the host lattice is transferring energy to the dopant ions. The emission spectra of the undoped nanocomposite in Fig. 6(a) was obtained by exciting the samples at 211 and 275 nm. The spectra present a broad exciton emission peak centered at 406 nm, ascribed to intrinsic defects within the ZnO and ZrO_2 lattices. The Gaussian fit of the broad band in Fig. 6(b) shows four overlapping peak maxima at 356, 406, 434 and 500 nm. The peaks at 356 and 500 nm were attributed to the near band and the V_o/O_i induced state emissions in ZnO, respectively [53]. Selvam et al. [54] attributed the 406, 434 and 500 nm to deep trap state emissions due to the recombination of the electron−hole pairs from localized deep level states in the bandgap. An estimate of the energy bandgap from PL at the host emission of 406 nm has a value of 3.05 eV for the undoped sample, which agrees quite well with the values obtained from UV spectroscopy in Fig. 5(b).

Figure 7(a) shows the excitation spectra at 481 nm while (b) shows the emission spectra of the Dy^{3+} -doped nanocomposites excited at 211 nm. Just as in the undoped samples, the excitation spectra have three peaks at 211, 275 and 400 nm. The emission spectra consist of the host emission

OSA CONTINUUM

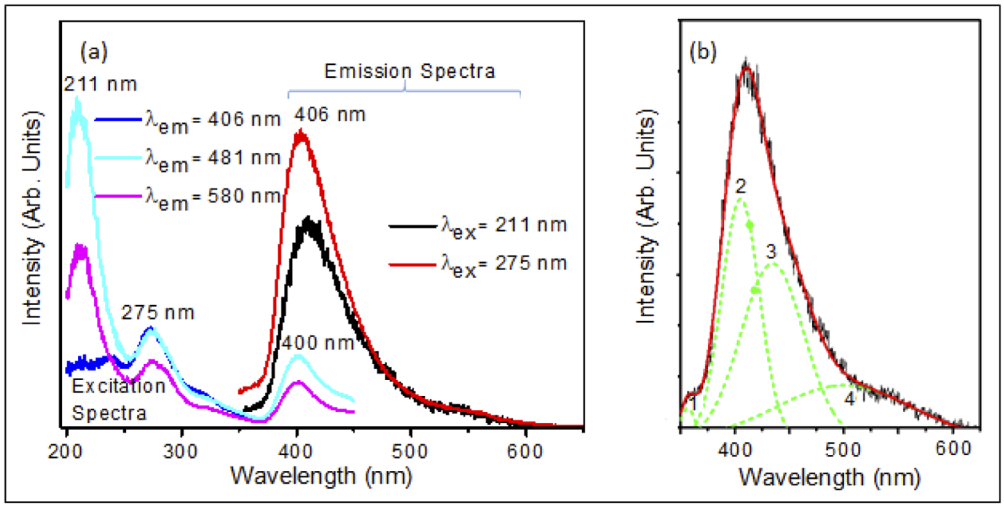

Fig. 6. (a) Excitation and emission spectra of the undoped sample (b) deconvoluted emission spectrum of the undoped sample.

band whose maxima is centered at 406 nm and the Dy^{3+} intra-configurational transition lines at 481 and 580 nm. The dominant 481 nm (blue) peak is ascribed to the hypersensitive electric dipole ($^4F_{9/2} \rightarrow {}^6H_{13/2}$) transition, while the yellow emission peak at 580 nm is assigned to magnetic dipole ($^4F_{9/2} \rightarrow {}^6H_{15/2}$) transition of Dy^{3+} [55,56]. The emission intensities of $^4F_{9/2} \rightarrow {}^6H_{13/2}$ transition in nanocomposite samples are greater than the $^4F_{9/2} \rightarrow {}^6H_{15/2}$ transition (Fig. 7(a)), showing very little deviation from an inversion symmetry [57]. According to Diaz-Torres et al., [55], the ratio between the intensities of these two peaks is known as the asymmetric ratio, *R*. *R* is used in determining the site symmetry or estimate the structural changes around the Dy^{3+} ions as well as the covalency of the bonds involving the oxygen ions. The asymmetry ratio, *R* for the composites was calculated using Eq. (5) [58];

$$R = \frac{\int I(^4F_{9/2} \rightarrow {}^6H_{13/2})dv}{\int I(^4F_{9/2} \rightarrow {}^6H_{15/2})dv} \tag{5}$$

where $\int I(^4F_{9/2} \rightarrow {}^6H_{13/2})dv$ and $\int I(^4F_{9/2} \rightarrow {}^6H_{15/2})dv$ are the integrated intensities of the hypersensitive transition and magnetic dipole transition, respectively.

Table 2 shows the calculated values of *R*, at the various concentrations of the Dy^{3+} doping in the nanocomposites. It has been shown that whenever the site occupied by the Dy^{3+} ions is highly symmetrical, the *R* value is low, whereas high values of *R* results from lower symmetry. Table 2 shows low values of *R*, (1.95–2.28) indicating a low symmetry around the Dy^{3+} sites in the nanocomposite, hence the electric dipole transition (blue) has the strongest intensity.

The intensities of the $^4F_{9/2} \rightarrow {}^6H_{13/2}$ and $^4F_{9/2} \rightarrow {}^6H_{15/2}$ transition peaks decreased with increasing Dy^{3+} concentrations indicating concentration quenching as a result of the shortened distance between activator ions (Dy^{3+} ions). At close proximity, energy is transferred among Dy^{3+} ions until it is absorbed by the lattice leading to the observed emission quenching. The critical distance, R_c is a threshold distance which defines the interaction mechanism of the concentration quenching and is defined by the relation [59];

$$R_c = 2\left(\frac{3V_x}{4\pi X_c N}\right)^{1/3} \tag{6}$$

OSA CONTINUUM

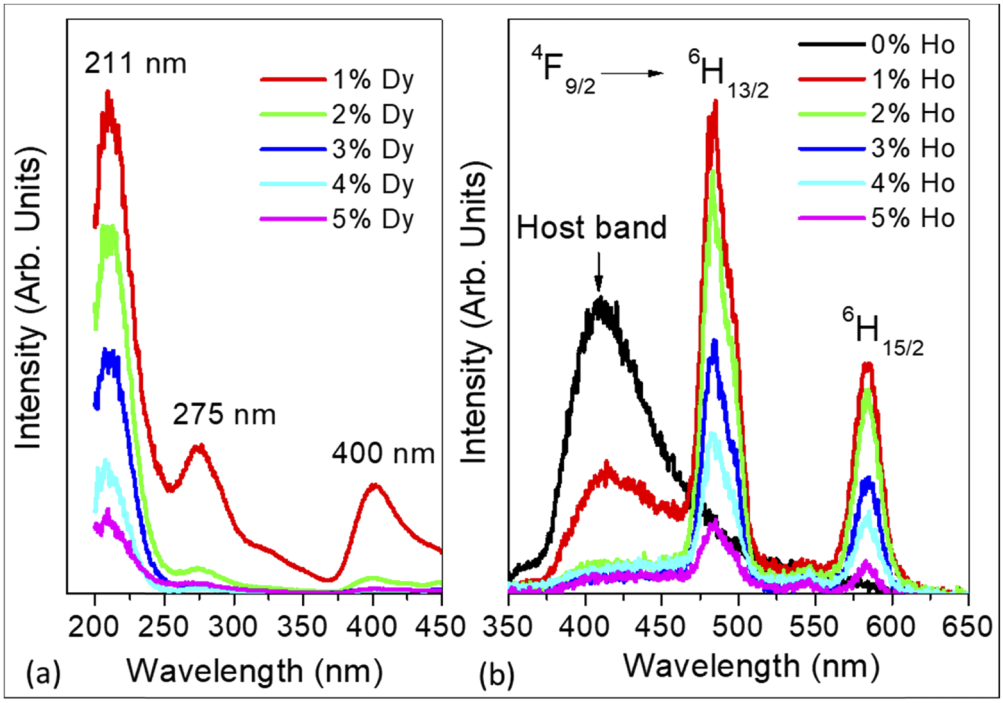

Fig. 7. (a) Excitation spectra of the Dy^{3+}-doped samples at $\lambda = 481$ nm and (b) Emission spectra of the samples at $\lambda = 211$ nm.

Table 2. CIE coordinates and asymmetry ratio of nanocomposites

Sample	CIE Coordinates		CCT (K)	Colour Purity %	Asymmetry Ratio, *R*
	x	*y*			
0%	0.165	0.103	2734	81.9	-
1%	0.250	0.265	17025	34.4	2.14
2%	0.271	0.315	9581	22.3	2.06
3%	0.258	0.301	11516	27.9	2.16
4%	0.242	0.285	14974	34.6	1.95
5%	0.201	0.239	51318	52.9	2.28

where V_x is the unit cell volume; in this case 49.970 $Å^3$ for ZnO and 132.514 $Å^3$ for ZrO_2, N is the number of cationic sites available in the unit cell of the nanocomposite, in which $N = 4$ for both hexagonal ZnO and cubic ZrO_2. Finally, the critical concentration, X_c of the Dy^{3+} ions, is the concentration at which the luminescence intensity of sensitizer is half that of sample without the activator. Since Dy^{3+} ions were excited through the host excitation band wavelength at 211 nm (Fig. 7(b)), the emission from Dy^{3+} is as a result of the transfer of energy from the host to the activator (Dy^{3+}) ion. Therefore, the critical concentration, X_c was obtained by plotting the emission intensity verses the concentration of Dy^{3+} ions as shown in Fig. 8. From the figure, the point at which the Dy^{3+} concentration axis for the host emission intensity is half that of the sample without Dy^{3+} ion is the critical activator ion concentration and its value was found to be 0.64%. There are basically two energy transfer mechanisms responsible for the concentration quenching; the exchange interaction which takes place at short distances below 5 Å and multipole interaction at distances larger than 5 Å. The calculated R_c values are 15.5 Å and 21.4 Å for ZnO

OSA CONTINUUM

and ZrO_2 in the nanocomposite, effectively ruling out the possibility of exchange interaction as the energy transfer process.

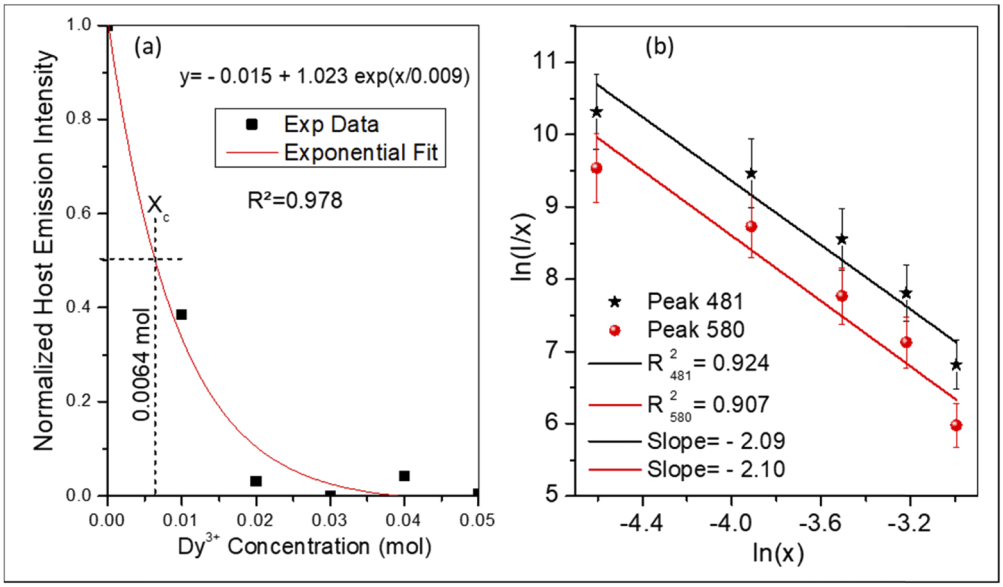

Fig. 8. (a) Dependence of the host emission band intensity on Dy^{3+} concentration and (b) fitting line of ln(I/x) versus ln(x) in nanocomposite.

According to Dexter's theory of energy transfer, [60–62], multipolar interaction can be determined by the relationship: -

$$\frac{I}{x} = k[1 + \beta\,(x)^{\theta/3}]^{-1} \tag{7}$$

where x is Dy^{3+} ion concentration (usually greater than the critical concentration, X_c), I/x is the emission intensity per concentration, k and β are constants dependent on the host lattice and θ is a function of multipolar character; whose values are $\theta = 6$, 8, 10 for dipole-dipole (d-d), dipole-quadrupole (d-q) and quadrupole-quadrupole (q-q) interactions, respectively. Using natural logarithms, Eq. (7) was reduced to a linear relationship and plotted in Fig. 8(b). From the equation, the slope of the linear fit of ln(I/x) verses ln(x) is equivalent to $-\theta/3$ and has values of −2.09 and −2.10 for the $^4F_{9/2} \rightarrow {}^6H_{13/2}$ (481 nm) and $^4F_{9/2} \rightarrow {}^6H_{15/2}$ (580 nm) transitions. Thus, θ was evaluated as 6.3, showing that the major energy transfer process responsible for the luminescence quenching in the nanocomposites was the dipole-dipole interaction between Dy^{3+} ions.

Therefore, the quenching at the high Dy^{3+} doping ratios is due to the energy transfer amongst the dopant ions arising from the reduced distances between the ions [63]. However, enhanced defect levels arising from the dopant oxygen vacancies, that act as charge traps in the lattice may lead to quenching [64]. The incorporation of Dy^{3+} ions in the composite may as well populate deep level non-radiative defects in the host matrix with enhanced doping.

Figure 9 shows the Commission International de I'Eclairage (CIE) coordinates [65] for the nanocomposites. From the PL spectra data, the chromaticity coordinates, the correlated colour temperature (CCT) and the colour purity of the Dy^{3+} doped composites were calculated at various concentrations and presented in Table 2. The coordinates of the undoped composite are in the violet region, while those of the doped samples are in the light blue region, with an advancement towards white light with enhanced doping. The CCT column in Table 2 shows that

OSA CONTINUUM

higher temperature radiations are emitted from the surfaces having enhanced doping. This is in agreement with studies which have shown that dysprosium has a dominant emission in the blue region [66]. Due to the dependence of the emissions on the dopant concentrations, the phosphors can, therefore, be tuned for use as sensors and blue LEDs as well as efficient light applications such as display systems.

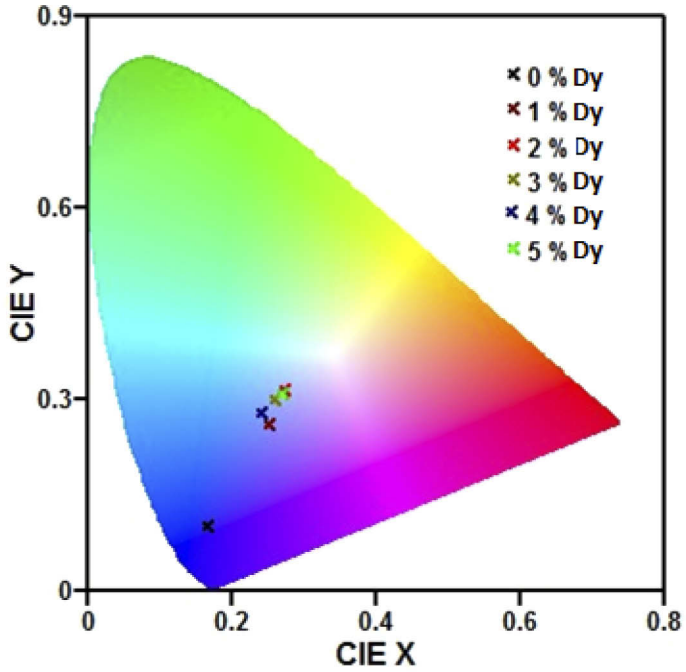

Fig. 9. CIE coordinate diagram of the composite showing the colours emitted at various doping percentages.

3.5. *Lifetime measurements*

Luminescence decay analysis can be used to obtain the energy transfer and quenching mechanisms within a material. Figure 10(a) shows the decay lifetimes of the 481 nm Dy^{3+} emissions when the samples were excited at a wavelength of 211 nm while Fig. 10(b) shows the normalized half-log decay curves. The non- linearity of the half-log plot shows that the decay was multiexponential and hence subsequently fitted into a bi-exponential function. According to Kumari and Manam [58], a bi-exponential decay may be expressed as;

$$I(t) = I_0 + A_1 e^{-t/\tau_1} + A_1 e^{-t/\tau_2} \tag{8}$$

The average decay lifetime, $< t >$ is expressed as,

$$<t> = \frac{A_1 {\tau_1}^2 + A_2 {\tau_2}^2}{A_1 \tau_1 + A_2 \tau_1} \tag{9}$$

where $I(t)$ is the luminescence intensity at time t, A_1 and A_2 are weighted constants, τ_1 and τ_2 are short and long decay components of the lifetimes, respectively. The long decay time is attributed to the dopant ions entrenched at the core of the crystallite site while the short decay time is associated with the dopant ions at the surface or near defect sites such as interstitials [67].

OSA CONTINUUM

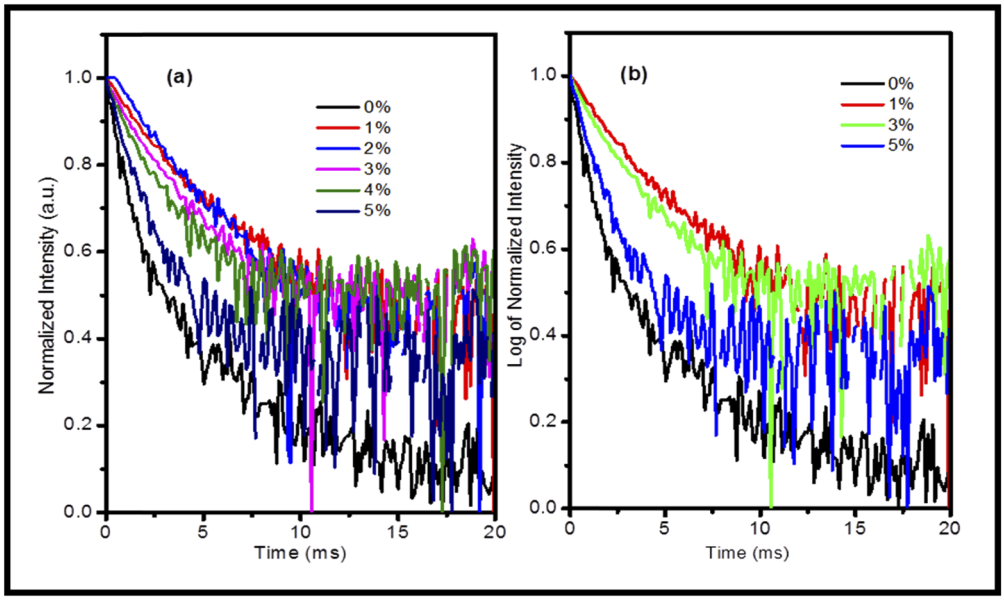

Fig. 10. (a) Normalized decay lifetime (b) half-log plot of decay lifetime of the nanocomposite.

Table 3 shows the average decay lifetimes $< t >$, of the doped samples. It was observed that the lower dopant ratios had higher lifetime values than the other samples. The reducing lifetimes on increased doping are an indication of non-radiative energy transfer from the host matrix to Dy^{3+} ions at or near the surface [67,68]. It can be concluded that the dopant ions segregated out onto the surface or interstitials in agreement with the XRD results and the decreased luminescence observed from enhanced doping.

Table 3. Average lifetimes of the samples excited at 211 nm to emit at a wavelength of 481 nm

Dysprosium conc./mol	0%	1%	2%	3%	4%	5%
Average lifetime <*t*> (ms)	4.80	8.18	5.47	4.01	3.24	3.10

4. Conclusion

Dysprosium - doped zinc zirconate composites were synthesized successfully using the solution combustion route. In this synthesis, zirconium butoxide and citric acid fuel were used. The composite consisted of mixed phases of cubic zirconia and hexagonal zinc oxide nanocrystals. These composites showed a tunable energy band gap lying between 2.99 and 3.07 eV. The doped samples exhibited varied PL spectra with the major excitation and emission peaks observed at 211 nm and 481 nm, respectively. The synthesized phosphors emit in deep blue region advancing towards white light as the Dy^{3+} concentration increases. The nanocomposite phosphors can be used in sensors, LEDs and the display technology.

Funding

National Research Foundation.

OSA CONTINUUM

Acknowledgments

We are grateful to the University of the Free State and the National Research Foundation, NRF for facilitating the study.

Disclosures

The authors declare no conflict of interest.

References

1. M. H. Habibi and E. Askari, "Fabrication and Spectral Properties of Zinc Zirconate Nanorod Composites by Sol-Gel Method for Optical Applications: Effect of Chloride and Oxychloride Precursors and Sintering Temperature on Band Gap," Synth. React. Inorg., Met.-Org., Nano-Met. Chem. **45**(2), 281–285 (2015).
2. R. Vittala and K.-C. Ho, "Zinc oxide based dye-sensitized solar cells: A review," Renewable Sustainable Energy Rev. **70**, 920–935 (2017).
3. V. Sugathan, E. John, and K. Sudhakar, "Recent improvements in dye sensitized solar cells: A review," Renewable Sustainable Energy Rev. **52**, 54–64 (2015).
4. M. H. Habibi and E. Askari, "Preparation of a Novel Zinc Zirconate Nanocomposite Coated on Glass for Removal of a Textile Dye (Reactive Brilliant Red X8B) From Water," Synth. React. Inorg., Met.-Org., Nano-Met. Chem. **45**(10), 1457–1462 (2015).
5. E. T. Thostenson, C. Li, and T.-W. Chou, "Nanocomposites in context," Compos. Sci. Technol. **65**(3-4), 491–516 (2005).
6. P. Palmero, "Structural Ceramic Nanocomposites: A Review of Properties and Powders' Synthesis Methods," Nanomaterials **5**(2), 656–696 (2015).
7. M. H. Habibi, E. Askari, M. Habibi, and M. Zendehdel, "Novel nanostructure zinc zirconate, zinc oxide or zirconium oxide pastes coated on fluorine doped tin oxide thin film as photoelectrochemical working electrodes for dye-sensitized solar cell," Spectrochim. Acta, Part A **104**, 197–202 (2013).
8. R. F. Marcomini, D. P. F. de. Souza, M. Kleitz, L. Dessemond, and M. Kleitz, "Blocking Effect of ZnO in YSZ/ZnO Composites," ECS J. Solid State Sci. Technol. **1**(6), N127–N134 (2012).
9. R. Narayan, "Use of nanomaterials in water purification," Mater. Today **13**(6), 44–46 (2010).
10. C. Santhosh, V. Velmurugan, G. Jacob, S. K. Jeong, A. N. Grace, and A. Bhatnagar, "Role of nanomaterials in water treatment applications: A review," Chem. Eng. J. **306**, 1116–1137 (2016).
11. Y. Zhang, B. Wu, H. Liu, H. Xu, M. Wang, Y. He, and B. Pan, "Nanomaterials-enabled water and wastewater treatment," NanoImpact **3-4**, 22–39 (2016).
12. D. Nohavica and P. Gladkov, "Zno nanoparticles and their applications – new achievments," in *Nanocon 2010*, Czech Republic, EU, Olomouc, 2010, p. 534.
13. R. Nielsen and T. Chang, "Zirconium and Zirconium Compounds," ed Wiley-VCH Verlag GmbH & Co. KGaA, Weinheim, 2005, 2–17.
14. S. Divya and M. P. Rani, "Phase and optical analysis of synthesized dysprosium doped zirconia," in *International Conference on Nanotechnology: The Fruition of Science*, 2017, 179–185.
15. I. Ahemen and F. B. Dejene, "Photophysical and energy transfer processes in Ce^{3+} co-doped ZrO2: Eu^{3+} nanorods," Appl. Phys. A **123**(2), 140 (2017).
16. J. P. Feist and A. L. Heyes, "Europium-doped yttria-stabilized zirconia for high-temperature phosphor thermometry," in *Proceedings of the Institution of Mechanical Engineers, Part L*, 2000, pp. 7–12.
17. I. Ahemen, F. B. Dejene, and R. Botha, "Strong green-light emitting Tb^{3+} doped tetragonal ZrO_2 nanophosphors stabilized by Ba^{2+} ions," J. Lumin. **201**, 303–313 (2018).
18. Y. S. Vidya, K. S. Anantharaju, H. Nagabhushana, S. C. Sharmad, H. P. Nagaswarupa, S. C. Prashantha, C. Shivakumara, and Danithkumar, "Combustion synthesized tetragonal ZrO_2-Eu^{3+}nanophosphors-Structural and photoluminescence studies," Spectrochim. Acta, Part A **135**, 241–251 (2015).
19. D. Kouyate, J.-C. Ronfard-Haret, and J. Kossanyi, "Photo- and electro-luminescence of rare earth-doped semi-conducting zinc oxide electrodes; Emission from both the dopant and the support," J. Lumin. **50**(4), 205–210 (1991).
20. S. Agrawal and V. Dubey, "Synthesis and characterization of rare earth doped nanophosphors," in *AIP Conference Proceedings* 2014.
21. S. Hoenderdaal, L. T. Espinoza, F. Marscheider-Weidemannb, and W. Graus, "Can a dysprosium shortage threaten green energy technologies?" Energy **49**, 344–355 (2013).
22. A. Elshkaki and T. E. Graedel, "Dysprosium, the balance problem, and wind power technology," Appl. Energy **136**, 548–559 (2014).
23. A. D. Watson, "The use of gadolinium and dysprosium chelate complexes as contrast agents for magnetic resonance imaging," J. Alloys Compd. **207-208**, 14–19 (1994).
24. G. Liu, K. Chen, and J. Li, "Combustion synthesis: An effective tool for preparing inorganic materials," Scr. Mater. **157**, 167–173 (2018).

OSA CONTINUUM

25. A. R. West, *Solid State Chemistry and its Applications*, Second Edition, Student Edition ed. Department of Materials Science and Engineering, University of Sheffield, John Wiley & Sons, Ltd, UK, 2005.
26. V. C. Milos Petrovic and S. Ramakrishna, "Perovskites: Solar cells & engineering applications – materials and device developments," Sol. Energy **122**, 678–699 (2015).
27. F. Deganello, G. Marcì, and G. Deganello, "Citrate–nitrate auto-combustion synthesis of perovskite-type nanopowders: A systematic approach," J. Eur. Ceram. Soc. **29**(3), 439–450 (2009).
28. K. C. Patil, S. T. Aruna, and T. Mimani, "Combustion synthesis: an update," Curr. Opin. Solid State Mater. Sci. **6**(6), 507–512 (2002).
29. A. S. Mukasyan, P. Epstein, and P. Dinka, "Solution combustion synthesis of nanomaterials," Proc. Combust. Inst. **31**(2), 1789–1795 (2007).
30. Arvind Varma, A. S. Mukasyan, A. S. Rogachev, and K. V. Manukyan, "Solution Combustion Synthesis of Nanoscale Materials," Chem. Rev. **116**(23), 14493–14586 (2016).
31. T. Mimani and K. C. Patil, "Solution combustion synthesis of nanoscale oxides and their composites," Mater. Phys. Mech. **4**, 134–137 (2001).
32. A. Alves, C. P. Bergmann, and F. A. Berutti, "Novel Synthesis and Characterization of Nanostructured Materials," in *Combustion Synthesis*, Springer-Verlag, Ed., 2013 ed. Springer-Verlag Berlin Heidelberg 2013: Springer, 2013, 11–20.
33. M. H. Habibi and E. Askari, "Thermal and structural studies of zinc zirconate nanoscale composite derived from sol–gel process. The effects of heat-treatment on properties," J. Therm. Anal. Calorim. **111**(1), 227–233 (2013).
34. X. Zhu, J. Zhou, J. Zhu, Z. Liu, Y. Li, and T. Al-Kassab, "Structural Characterization and Optical Properties of Perovskite $ZnZrO_3$ Nanoparticles," J. Am. Ceram. Soc. **97**(6), 1987–1992 (2014).
35. I. Ahemen and F. B. Dejene, "Site spectroscopy probing of Eu^{3+} incorporated into novel $LiY_xSr_yZrO^{3+\alpha}$ host matrix," Curr. Appl. Phys. **18**(11), 1359–1367 (2018).
36. M. K. Musembi and F. B. Dejene, "Investigation of the effect of precursor ratios on the solution combustion synthesis of zinc zirconate nanocomposite," Heliyon **5**(12), e03028 (2019).
37. Y. Sa, Y. Guo, X. Feng, M. Wang, P. Li, Y. Gao, X. Yang, and T. Jiang, "Are different crystallinity-index-calculating methods of hydroxyapatite efficient and consistent?" New J. Chem. **41**(13), 5723–5731 (2017).
38. P. Corradini, F. Auriemma, and C. D. Rosa, "Crystals and Crystallinity in Polymeric Materials," Acc. Chem. Res. **39**(5), 314–323 (2006).
39. R. D. Shannon and C. T. Prewitt, "Effective Ionic Radii in Oxides and Fluorides," Acta Crystallogr., Sect. B: Struct. Crystallogr. Cryst. Chem. **25**(5), 925–946 (1969).
40. Y. Q. Jia, "Crystal Radii and Effective Ionic Radii of the Rare Earth Ions," J. Solid State Chem. **95**(1), 184–187 (1991).
41. K. Mondal and J. Manam, "Investigation of photoluminescence properties, thermal stability, energy transfer mechanisms and quantum efficiency of $Ca_2ZnSi_2O_7$: Dy^{3+}, Eu^{3+} phosphors," J. Lumin. **195**, 259–270 (2018).
42. C. Shivakumara, R. Saraf, and P. Halappa, "White luminescence in Dy^{3+} doped BiOCl phosphors and their Judd-Ofelt analysis," Dyes Pigm. **126**, 154–164 (2016).
43. S. Velumania, X. Mathewa, P. J. Sebastiana, S. K. Narayandassb, and D. Mangalarajb, "Structural and optical properties of hot wall deposited CdSe thin films," Sol. Energy Mater. Sol. Cells **76**(3), 347–358 (2003).
44. P. Gupta and M. Ramrakhiani, "Influence of the Particle Size on the Optical Properties of CdSe Nanoparticles," Open Nanosci. J. **3**(1), 15–19 (2009).
45. D. B. Yram, "Investigating the Optical Band Gap and Crystal Structure of Copper Sulphide and Copper Selenide Thin Films Deposited by Chemical Bath Deposition," Mat. Res. **18**(5), 1000–1007 (2015).
46. A. Rahdar, M. Aliahmad, and Y. Azizi, "NiO Nanoparticles Synthesis and Characterization," Journal of Nanostructures **5**, 145–151 (2015).
47. Arkajit, Arghya, Sucharita, and Tarit, "Solid State Calistry Calculator," ed, 2015.
48. T. Ungár, E. Schafler, and J. Gubicza, "Bulk Nanomaterials Materials," in *Bulk Nanostructured Intermetallic Alloys Studied by Transmission*, M. J. Zehetbauer and Y. T. Zhu, eds. WILEY-VCH Verlag GmbH & Co. KGaA, 2009, 361–383.
49. H.-W. Chen, H. Sun, H.-W. Zhang, T.-C. Zhou, B.-W. Zhang, J.-F. Zhang, and X.-L. Tang, "Low-temperature sintering and microwave dielectric properties of $(Zn^{1-x}Co^{x})^{2}SiO^{4}$ ceramics," Ceram. Int. **40**(9), 14655–14659 (2014).
50. N. M. Rasdi, Y. W. Fen, N. A. S. Omara, R. S. Azis, and M. H. M. Zaid, "Effects of cobalt doping on structural, morphological, and optical properties of Zn2SiO4 nanophosphors prepared by sol-gel method," Results Phys. **7**, 3820–3825 (2017).
51. V. R. Akshay, B. Arun, G. Mandal, and M. Vasundhara, "Impact of Mn-dopant concentration in observing narrowing of band-gap, urbach tail and paramagnetism in anatase TiO2 nanocrystals," New J. Chem. **43**(37), 14786–14799 (2019).
52. I. Ahemen and F. B. Dejene, "Luminescence and energy transfer mechanism in Eu^{3+}-Tb^{3+}-co-doped ZrO2 nanocrystal rods," J. Nanopart. Res. **19**(1), 6 (2017).
53. R. K. Biroju and P. K. Giri, "Strong visible and near infrared photoluminescence from ZnO nanorods/nanowires grown on single layer graphene studied using sub-band gap excitation," J. Appl. Phys. **122**(4), 044302 (2017).
54. N. C. S. Selvam, J. J. Vijaya, and L. J. Kennedy, "Effects of Morphology and Zr Doping on Structural, Optical, and Photocatalytic Properties of ZnO Nanostructures," Ind. Eng. Chem. Res. **51**(50), 16333–16345 (2012).

OSA CONTINUUM

55. L. A. Diaz-Torres, E. De la Rosa, P. Salas, V. H. Romero, and C. Angeles-Chávez, "Efficient photoluminescence of Dy^{3+} at low concentrations in nanocrystalline ZrO_2," J. Solid State Chem. **181**(1), 75–80 (2008).
56. A. Baéz-Rodríguez, O. Alvarez-Fragoso, M. García-Hipólito, J. Guzmán-Mendoza, and C. Falcony, "Luminescent properties of ZrO2:Dy^{3+} and ZrO_2:Dy^{3+}+Li^+ films synthesized by an ultrasonic spray pyrolysis technique," Ceram. Int. **41**(5), 7197–7206 (2015).
57. Z. Yang, H. Dong, X. Liang, C. Hou, L. Liub, and F. Lua, "Preparation and fluorescence properties of color tunable phosphors $Ca_3Y_2(Si_3O_9)_2$:Dy^{3+}," Dalton Trans. **43**(30), 11474–11478 (2014).
58. P. Kumari and J. Manam, "Structural, optical and special spectral changes of Dy^{3+} emissions in orthovanadates," RSC Adv. **5**(130), 107575 (2015).
59. I. E. Kolesnikov, A. A. Kalinichev, M. A. Kurochkin, E. V. Golyeva, A. S. Terentyeva, E. Y. Kolesnikov, and E. Lähderanta, "Structural, luminescence and thermometric properties of nanocrystalline YVO_4:Dy^{3+} temperature and concentration series," Sci. Rep. **9**(1), 2043 (2019).
60. L. G. V. Uitert and L. F. Johnson, "Energy Transfer Between Rare-Earth Ions," J. Chem. Phys. **44**(9), 3514–3522 (1966).
61. A. Krishnan, T. S. Sreeremya, A. P. Mohamed, U. S. Hareesha, and S. Ghosh, "Concentration quenching in cerium oxide dispersions via a Forster resonance energy transfer mechanism facilitates the identification of fatty acids," RSC Adv. **5**(30), 23965–23972 (2015).
62. B. Tian, B. Chen, Y. Tian, J. Sun, X. Li, J. Zhang, H. Zhong, L. Cheng, and R. Hua, "Concentration and temperature quenching mechanisms of Dy^{3+} luminescence in $BaGd_2ZnO_5$ phosphors," J. Phys. Chem. Solids **73**(11), 1314–1319 (2012).
63. R. C. Martínez-Olmos, J. Guzmán-Mendoza, A. Báez-Rodríguez, O. Álvarez-Fragoso, M. García-Hipólito, and C. Falcony, "Synthesis, characterization and luminescence studies in ZrO^2:Dy^{3+} and ZrO_2:Dy^{3+}, Gd^{3+} films deposited by the Pyrosol method," Opt. Mater. **46**, 168–174 (2015).
64. S. V. Motloung, F. B. Dejene, H. C. Swart, and O. M. Ntwaeaborwa, "Effects of Cr^{3+} mol% on the structure and optical properties of the $ZnAl_2O_4$:Cr^{3+} nanocrystals synthesized using sol-gel process," Ceram. Int. **41**(5), 6776–6783 (2015).
65. P. Patil. (2010, 06/09/2019). *CIE Coordinate Calculator*. Available: https://www.mathworks.com/matlabcentral/fileexchange/29620-cie-coordinate-calculator
66. B. Grobelna, A. Synak, and P. Bojarski, "The luminescence properties of dysprosium ions in silica xerogel doped with $Gd_{1.6}Dy_{0.4}(WO_4)_3$," Opt. Appl. **42**(2), 337–344 (2012).
67. I. Ahemen, F. B. Dejene, R. E. Kroon, and H. C. S. b, "Effect of europium ion concentration on the structural and photoluminescence properties of novel Li_2BaZrO_4:Eu^{3+} nanocrystals," Opt. Mater. **74**, 58–66 (2017).
68. Y. Zhang, W. Gong, J. Yu, Z. Cheng, and G. Ning, "Multi-color luminescence properties and energy transfer behaviors in host-sensitized $CaWO_4$:Tb^{3+}, Eu^{3+} phosphors," RSC Adv. **6**(37), 30886–30894 (2016).